Anomalous refraction, diffraction, and imaging in metamaterials

Thomas Paul,* Carsten Rockstuhl, Christoph Menzel, and Falk Lederer
Institute of Condensed Matter Theory and Solid State Optics, Friedrich-Schiller-Universität Jena, Max-Wien-Platz 1, D-07743 Jena, Germany

(Received 12 August 2008; revised manuscript received 28 January 2009; published 23 March 2009)

In the past several years, optical metamaterials (MMs) have attracted a considerable deal of interest because it may be anticipated that their properties can be shaped to an unprecedented extent relieving optics from some of its natural limitations. An inevitable first step toward this goal is the evaluation of the optical properties of specifically designed MMs. To date, apart from identifying chiral properties of very specific configurations, this is primarily done in retrieving an effective refractive index—mostly—only for normal incidence. On this basis suggestions for a perfect lens, exploiting this negative refractive index have been put forward by taking advantage of geometrical optics arguments. We show that this approach is pointless for realistic MMs. Instead we prove that the *dispersion relation* of normal modes in these MMs provides all the required information. Most of the relevant optical parameters, such as refraction and diffraction coefficients, can be derived from this relation. Imaging properties follow straightforwardly from that data. This general approach holds for any optical material, in particular, for all MMs in question. As an example, we apply it to the fishnet structure: one of the most prominent and best studied design approaches to date. We show that both refraction and diffraction properties are strongly spatially and temporally dispersive and they can even change sign. In detail, we study the effect of these peculiarities on imaging and refraction of finite beams. In particular, we discuss both the effect of the specific dispersion relation and the losses on the imaging properties. All our physical predictions are backed by rigorous numerical calculations and the agreement is almost perfect. Ultimately the main conclusion to be drawn is that a negative index of refraction is by no means a sufficient criterion to achieve negative refraction and/or perfect imaging.

DOI: 10.1103/PhysRevB.79.115430 PACS number(s): 78.20.Ci, 75.30.Kz, 73.20.Mf, 41.20.Jb

I. INTRODUCTION

Optical metamaterials (MMs) are a class of artificial matter that primarily derive its properties from intentionally designed geometrical features of periodically arranged unit cells rather than from the intrinsic material properties of its constituents. Exploiting this freedom in design, MMs are expected to have the potential to realize promising optical devices with unprecedented properties and numerous applications such as the perfect lens[1] or the cloaking device.[2] At present, the description of light propagation in such media is frequently simplified. This simplification relies on the argument that the spatial details of the unit cells are not resolved by the propagating field if $\lambda \gg a_c$, where a_c is a characteristic length of the underlying nanostructure, i.e., the unit-cell size. In this case, the medium is effectively homogenized and the fairly cumbersome rigorous description of light propagation can be avoided by assigning effective parameters to the medium. Investigating the reflection/transmission behavior both an effective refractive index and an effective impedance can be calculated.[3,4] In a second step, these parameters, which are related to a propagating wave in a *definite direction* (to date almost exclusively normal to the MM surface), are used to straightforwardly derive the effective permittivity ε and permeability μ.

However, this approach contains some inherent deficiencies. First, optical MMs operate in a mesoscopic domain, which is characterized by a size of the unit cell that is smaller than—but yet—on the order of the wavelength. This leads inevitably to the effect that the optical response at a certain site depends both on the field and its derivative at this site, being an indication for spatial dispersion. Second, all effective parameters derived are related to a certain direction of wave propagation,[5–7] which means that they are not globally valid for a certain MM. Hence, aiming at describing any optical functionality in MMs that requires off-axis propagation (such as imaging and cloaking), the full dispersion relation of the MM normal modes, i.e., the Bloch waves in periodic media, has to be evaluated. The dispersion relation $\omega(k_x,k_y,k_z)$ relates frequency and wave vector of these normal modes. An effective refractive index $n=\sqrt{k_x^2+k_y^2+k_z^2}/(\omega/c)$ can be easily derived by a simple scaling but yields no further information. As is well known from the light propagation in other periodically structured optical media like photonic crystals and waveguide arrays, effects such as refraction and diffraction for monochromatic fields, as elements of the image formation process, can be exactly and easily described by inspecting the dispersion relation at a fixed frequency ω_0 (isofrequency contour), e.g., $k_z(k_x,k_y,\omega_0)$. In doing so, anomalous effects such as negative and zero diffraction as well as negative refraction have been identified.[8,9] Here we aim at proceeding along this path by analyzing the dispersion relation for arbitrary transverse wave-vector components, i.e., propagation directions, and studying the consequences for refraction and diffraction in imaging MMs. From a general point of view, the image formation using a MM slab device requires the compensation of normal light diffraction in free space by anomalous light diffraction in the MM. Thus, an essential goal is to investigate the angularly and spectrally dependent *diffraction coefficient* of MMs. As shown earlier,[8,9] the diffraction coefficient is related to the curvature of the isofrequency surface. Its be-

 ©2009 The American Physical Society

havior provides the key for understanding the lensing property of MMs. In this respect, an optimal MM for imaging applications should exhibit an isofrequency curve with a constant negative curvature, i.e., a sphere. Only in this case, it is permitted and useful to assign a global and constant negative refractive index. Thus, dealing with mesoscopic MMs, it is not of any or only of minor importance to have a medium at hand with a large negative index of refraction that varies with the propagation direction. It will be shown that, although the MM exhibits a negative index in the entire angular spectral domain, the diffraction of a beam is normal and compares to that of a real homogeneous medium. It will be furthermore shown that the geometrical shift which a beam experiences upon traversing a MM slab, being a measure of wide beam refraction, can be either negative or positive; although the respective effective index is negative. The sign of this shift can be easily explained by the concrete shape of the isofrequency surface. Similar observations were already reported in Ref. 10.

The overall aim of this work is to show that the dispersion relation of the relevant normal modes in any optical material, particularly in MMs, is the key for understanding linear interactions of optical beams and pulses with matter. Our main conclusions are general. Although, the concrete numerical studies are performed for a three-dimensional (3D) fishnet structure, the derived conclusions are applicable for other types of MMs too, as there are, for example, indefinite MMs exhibiting hyperbolic isofrequency curves.[11,12] The rest of the paper is structured as follows. In Sec. II we calculate the dispersion relation and the isofrequency curves by using two different approaches. On this basis, we derive the relevant quantities for beam propagation such as an inclination and diffraction coefficient. In Sec. III the image formation by using a MM slab is predicted in taking advantage of these studies. These results are compared with fully numerical simulations. Finally, the refraction of wide beams at MM slabs is discussed in Sec. IV.

II. DISPERSION RELATION

Because our studies aim at spatial effects such as diffraction and image formation, we need to calculate the isofrequency curves, i.e., the dependence of the longitudinal on the transverse wave-vector components of the normal modes. In bulk MMs with periodically arranged unit cells, these normal modes are Bloch waves. In order to use these MMs as imaging devices, it has to be ensured that only the fundamental Bloch wave contributes to the transmitted field, i.e., the higher-order evanescent waves must suffer large losses. It has been shown that this condition usually holds for bulk fishnet MMs, whereas in stacked split-ring MMs additional measures are required to avoid contributions of these higher-order modes.[13] The procedure may be even further facilitated if the MM can be effectively homogenized. In this effectively homogeneous medium, the relevant normal modes are plane waves. The justification of treating the medium as an effective homogenous one can be evaluated in comparing the results of two distinct approaches. In the first approach, the exact one—the dispersion relation $k_z^{\mathrm{BM}}(k_x,k_y;\omega)$ of the fundamental Bloch mode in an infinite MM—is calculated. In the second approach, recently presented,[6] the relation $k_z^{\mathrm{PW}}(k_x,k_y;\omega)$ for plane waves in an effective homogeneous medium can be derived from the complex reflection and transmission coefficients of a finite MM slab for arbitrary transverse wave-vector components (k_x,k_y). This parameter retrieval represents an extension of the widely used normal-incident retrieval.[4] The reflection and transmission coefficients are rigorously computed by using the Fourier modal method (FMM) (Refs. 14–16) for a realized fishnet MM.[17] The latter approach has the advantage that no infinite medium is required, thus it meets better the experimental conditions. A comparison of these alternative approaches results in almost identical isofrequency curves provided that the MM thickness exceeds that of four fishnet layers.[7] Thus, in what follows, we have calculated the dispersion relation by taking advantage of the retrieval procedure for the finite slab.

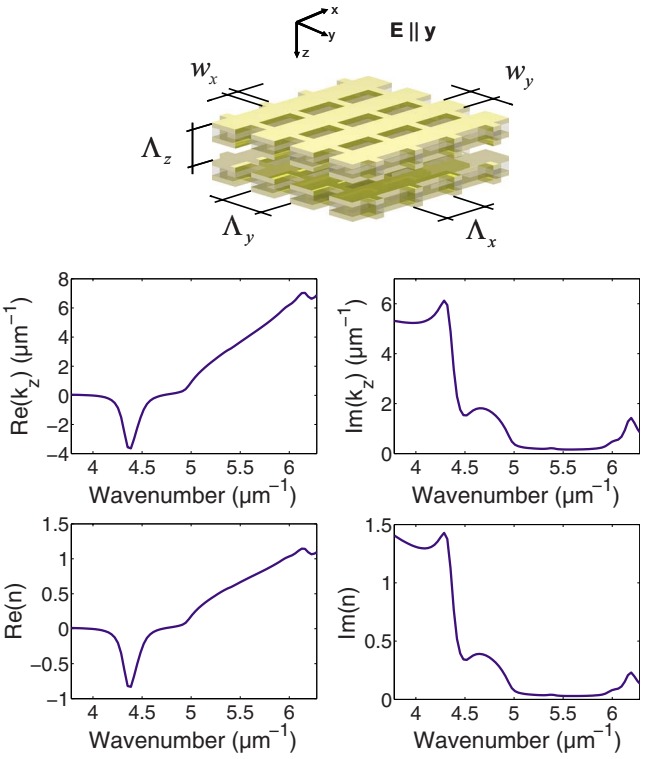

FIG. 1. (Color online) Top: sketch of the fishnet structure under consideration. Bottom: dispersion relation $k_z(2\pi\lambda^{-1})$ and the derived effective refractive index $n(2\pi\lambda^{-1})$ of the 12 layer fishnet MM for normal incidence.

As already mentioned, in order to get more specific with regard to available structures we have chosen the fishnet structure as an exemplary system (see the top in Fig. 1). At present it seems to be one of the most promising approaches obtaining a MM with the required anomalous refraction and diffraction properties at optical frequencies. Furthermore, it was recently shown that bulk fishnet MMs can be fabricated with available technologies.[18] The geometrical data are taken from the literature[17] and amount to $w_y=316$ nm, $w_x=100$ nm, $\Lambda_x=\Lambda_y=600$ nm, and $\Lambda_z=200$ nm. The fishnet itself consists of three layers; two metallic layers separated by a thin dielectric spacer. The metallic layers consist of

silver with a thickness of 45 nm. The permittivity ε_{Ag} is calculated using the Drude formula.[19] The dielectric spacer consists of MgF_2 with a thickness of 30 nm. Its refractive index is reasonably assumed to have no dispersion and amounts to 1.38 in the frequency region of interest. To ensure that the derived dispersion relation reflects that of the bulk (infinitely extended) MM (Ref. 13), 12 layers have been assumed for the retrieval. The remaining space in the unit cell in z direction is assumed to be occupied by air, ensuring that the extension of the unit cell in z direction amounts to Λ_z. Overall, the whole MM slab device is surrounded by air. It has to be noted that deviations from this material and geometric data affect the results only marginally and all physical conclusions will remain valid.

For the sake of simplicity we assume in the following that the transverse wave vector of the incident field has only one component k_x along the interface ($k_y \equiv 0$). Therefore, we restrict ourselves to scenarios with an x-z plane of incidence and a y-polarized electrical field. Thus, the polarization of the incident field is identical for all incident angles. For this polarization the excited structural plasmonic resonance, which provides the required magnetic properties, is strongest and occurs in the desired frequency domain. Resonances associated with an x-polarized electric field occur at higher frequencies and are irrelevant here. In general, other arrangements of the structure with respect to the illuminating field would be possible as well but will alter only quantitatively our conclusions.

Figure 1 shows the frequency dispersion $k_z(k_0=2\pi\lambda^{-1})$ (for practical reasons we use the vacuum wave number k_0 rather than the frequency) for normal incidence ($k_x=0$). It is evident that in a certain spectral domain ($4.0\ \mu m^{-1} \lesssim k_0 \lesssim 4.7\ \mu m^{-1}$), the real part of the longitudinal wave-vector component $\Re e(k_z)$ becomes negative. A formally defined effective refractive index $n=\sqrt{k_x^2+k_z^2}/k_0$ also exhibits a negative real part in this domain (see Fig. 1). It attains its minimum value at $4.37\ \mu m^{-1}$.

To proceed with the analysis of the spatial dispersion relation (isofrequency curves), we selected three frequencies where detailed investigations have been performed. The choice of frequencies was motivated by the spectral behavior of the propagation constant as shown in Fig. 1. The first value of $k_1=4.37\ \mu m^{-1}$ ($\lambda_1=1.437\ \mu m$) corresponds to the minimum of $\Re e(k_z)$ for normal incidence. The two other frequency values are slightly positively/negatively detuned from this spectral position, i.e., $k_2=4.52\ \mu m^{-1} > k_1$ ($\lambda_2=1.389\ \mu m$) and $k_3=4.23\ \mu m^{-1} < k_1$ ($\lambda_3=1.486\ \mu m$). The size of detuning permits a meaningful qualitative distinction in the angular behavior when compared to normal incidence. This size effects only quantitatively the observations. The corresponding dispersion relations (isofrequency curves) $k_z(k_x)$ are shown in Fig. 2. These curves are symmetric with respect to k_x, i.e., $k_z(k_x)=k_z(-k_x)$. In this figure, the above defined effective refractive index is also displayed to underline its strong variation with the transverse wave-vector component.

The k_x component of the wave vector is varied between zero and $4.2\ \mu m^{-1}$ which approximately corresponds to grazing incidence from air for the three wavelengths of interest. From Fig. 2 it can be seen that $\Re e(k_z)$ approaches zero

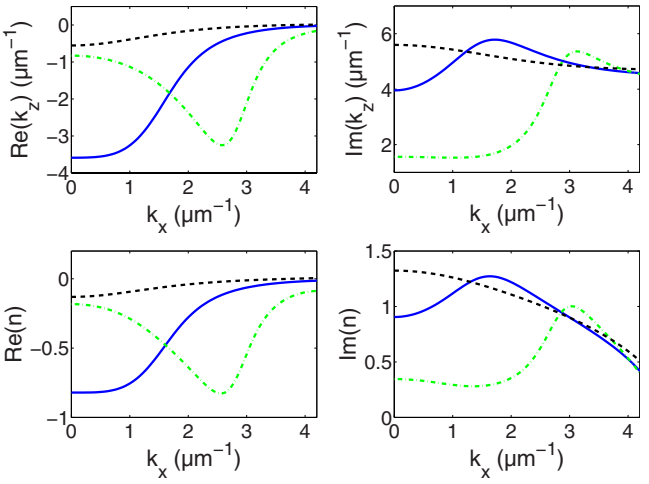

FIG. 2. (Color online) Dispersion relation (isofrequency curve) $k_z(k_x)$ and the effective refractive index $n(k_x)$. Blue, solid: $\lambda_1=1.437\ \mu m$; green, dashed dotted: $\lambda_2=1.389\ \mu m$; and black, dashed: $\lambda_3=1.486\ \mu m$. Due to the symmetry of the MM, all curves are mirror symmetric with respect to k_x

for $k_x \to 4.2\ \mu m^{-1}$ in all three cases. In this limit, the MM slab mimics just a diluted metal and does not support any magnetic resonance. Thus, also larger transverse wave vectors, which apply to evanescent waves of the exciting field and thus subwavelength structures, do not excite magnetic resonances at these wavelengths. Hence, the first important conclusion of this study is that information on subwavelength structures gets lost and a perfect lens cannot be obtained with this specific fishnet geometry.

Qualitatively, the real part $\Re e(k_z)$ for λ_1 (blue, solid) and λ_3 (black, dashed) behaves similar and the respective curves differ from each other only by a scaling factor. In particular, both curves exhibit their minimum at normal incidence ($k_x=0$) and vary monotonically with k_x. In stark contrast, for λ_2 the isofrequency curve $k_z(k_x)$ exhibits its minimum at $k_x \simeq 2.60\ \mu m^{-1}$ and the curve shows a nonmonotonic dependence on k_x, having dramatic consequences for the imaging properties.

III. DIFFRACTION OF BEAMS AND IMAGING PROPERTIES

A very promising and frequently invoked application of MMs is the perfect lens. This requires a MM slab with a unitary impedance, vanishing losses, and a refractive index of $\Re e(n)=-1$ for all transverse wave vectors k_x. If losses are not accounted for, it allows the production of a perfect image of a monochromatic source located in the front focus of the MM slab.[1,20] Let us briefly remind the basic properties of a MM acting as a perfect lens in terms of its dispersion relation (isofrequency contours). First, it has to exhibit a spherical isofrequency surface (at least at the operational wavelength) which provides a constant but anomalous diffraction in the propagating wave regime. Second, the amplification of evanescent waves is a pure surface-related effect which takes advantage of the surface states resulting in an effective and proper gain of all incident evanescent waves. These evanes-

cent waves are crucial for obtaining subwavelength resolution, which has been already proven in the microwave domain.[21] However, in our considerations we may disregard them because—as mentioned above—the fishnet structure under study does not exhibit any magnetic resonances for the respective large transverse wave vectors in the relevant spectral region. Furthermore, there is another more practical reason why we did not study their influence on image formation. The limitations imposed on the image quality by the imperfect (noncircular) dispersion relation exceed by far the possible effect of missing evanescent waves. In view of the above arguments, it will suffice to study the performance of a MM slab as a conventional lens, i.e., without the potential for subwavelength resolution. Thus it is of primary interest to analyze the consequences of the noncircular shape of the isofrequency surfaces as already displayed in Fig. 2.

In the following, we consider the image formation at two distinct frequencies. The choice was motivated by the preliminary results as discussed in Sec. II. First, we choose $\lambda_1 = 1.437\ \mu$m and second $\lambda_2 = 1.389\ \mu$m because these two cases turned out to exhibit quite remarkably different dispersion curves (see Fig. 2). Results for λ_3 would have been similar to λ_1, hence this wavelength is omitted.

To investigate its pertinent imaging properties, the field originating from a finite object at $z=0$ (the source position in front of the device) has to be propagated through the MM and the adjacent domains. In what follows, we assume a one-dimensional, TE-polarized ($\mathbf{E} = E\mathbf{e}_y$) finite field distribution of a line source as $E(x,0) = E_0(x)$. By using the angular decomposition of this field $E_0(k_x) = \frac{1}{2\pi}\int_{-\infty}^{+\infty} dx E_0(x)\exp(-ik_x x)$, its propagation to any position z behind the device can be represented by its angular spectrum as

$$\begin{aligned} E(x,z) &= \int_{-\infty}^{+\infty} dk_x\ E_0(k_x)\exp\{ik_z^{\mathrm{FS}}(k_x z_-)\}T(k_x) \\ &\quad \times \exp\{ik_z^{\mathrm{FS}}(k_x)(z-z_+)\}\exp(ik_x x) \\ &= \int_{-\infty}^{+\infty} dk_x\ E(k_x;z)\exp(ik_x x), \end{aligned} \tag{1}$$

with $k_z^{\mathrm{FS}}(k_x) = \sqrt{(\omega/c)^2 - k_x^2}$ (the propagation constant in free space), containing both homogeneous and evanescent components. Furthermore, z_- and z_+ denote the coordinates of the entrance and exit facets of the MM slab. $T(k_x)$ represents its transmission function relating the input and output fields by $E(k_x;z_+) = T(k_x)E(k_x;z_-)$. There are two approaches to derive this transmission function $T(k_x)$. The first one relies on the rigorous numerical propagation of every angular spectrum component through the actual nanostructure employing the FMM. Note that due to the small period of the fishnet structure, only the zeroth transmitted diffraction order is propagating, whereas the others are evanescent.

The second approach relates the dispersion relation $k_z(k_x)$ to an approximated transmission function referred to as $T_D(k_x)$. Provided that $T(k_x) \approx T_D(k_x)$, the dispersion relation can be exploited to predict and explain the imaging properties of the realistic MM slab. But, how to calculate T_D? Taking into account that the MM slab introduces a strong damping, it seems reasonable to assume at first that multiple reflections of light inside the slab can be neglected. Consequently, the propagation of a plane-wave eigenmode from the input to the output facet in the MM slab is given by a simple multiplication with the factor $\exp\{ik_z(k_x)d\}$, with d being the MM thickness. Neglecting furthermore the reflections at the MM boundaries, the entire transmission coefficient can be approximated by

$$T_D(k_x) = \exp\{ik_z(k_x)d\}. \tag{2}$$

Equation (2) provides the desired simple yet approximate relation between the dispersion relation and the transmission coefficient of the structure. To evaluate its validity, Figs. 3 and 4 show a comparison between $T(k_x)$ and $T_D(k_x)$ for both wavelengths of interest ($\lambda_1 = 1.437\ \mu$m and $\lambda_2 = 1.389\ \mu$m).

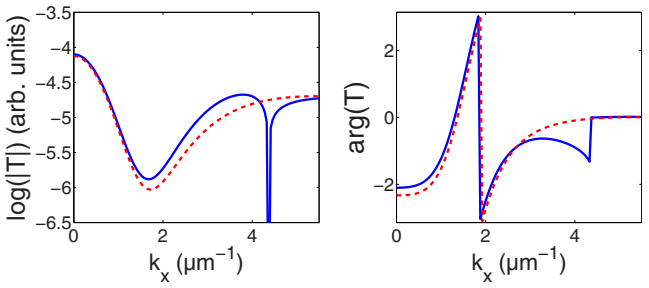

FIG. 3. (Color online) Logarithm of the modulus (left) and the phase (right) of the transmission coefficient vs k_x for $\lambda_1 = 1.437\ \mu$m. T—blue, solid curve; T_D—red, dotted curve.

In general, both models coincide very well for either wavelength. Only near grazing incidence where $|T(k_x)|$ tends to zero ($\log|T| \to -\infty$) also qualitative differences can be observed for the two approaches. We attribute these deviations to Fresnel effects at the MM interfaces neglected in calculating $T_D(k_x)$. We mention that all succeeding numerical studies concerning the MM imaging properties are performed in using the rigorously computed transmission coefficient $T(k_x)$. The dispersion relation, and thus $T_D(k_x)$, will be only used to back the numerical results by physical arguments. However, it will turn out that the results of both approaches agree perfectly.

Returning to Eq. (2) it is important to note that the approximated transmission coefficient $T_D(k_x)$ entirely mimics the propagation within a MM over a distance d. All information about refraction into the MM and diffraction inside the

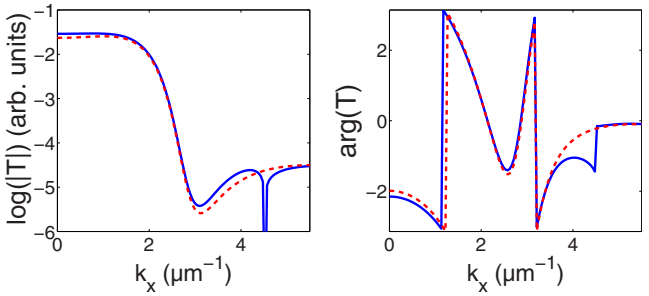

FIG. 4. (Color online) Logarithm of the modulus (left) and the phase (right) of the transmission coefficient vs k_x for $\lambda_1 = 1.389\ \mu$m. T—blue, solid curve; T_D—red, dotted curve.

MM are provided by the dispersion relation, or more precisely, the respective isofrequency curves. This concept has been successfully applied for various periodically structured media, such as photonic crystals and waveguide arrays, to explain effects such as superprism action and diffraction-free propagation.[8,9] Our aim is to apply this concept to MMs too, although the lossy characteristics of contemporary (optical) MMs will prevent a complete analogy. Proceeding along this route, we will shortly summarize the main ideas whereas adapted quantities, such as diffraction and refraction coefficients, are defined taking into account the lossy nature of the underlying media.

Therefore we assume that a monochromatic beam propagates in the positive z direction ($z+$) and is incident onto the three-dimensional MM. Its mean propagation direction is denoted by $\mathbf{k}^{(0)}=(k_x^0,k_z^0)^T$.

The propagation of the beam inside the MM is governed by the set of excited angular spectrum components. For lossless media, the curvature of the isofrequency curve represents a measure for the sign and strength of diffraction. Thus we may define a diffraction coefficient (in analogy to the dispersion coefficient in the temporal domain) as

$$D(\mathbf{k}^{(0)}) = \left.\frac{d^2\mathfrak{Re}(\mathbf{k})}{ds^2}\right|_{\mathbf{k}^{(0)}}, \tag{3}$$

with $ds=|d\mathbf{k}|$. This rather general definition translates into the more convenient form

$$D(k_x^0) = \left.\frac{\dfrac{\partial^2\mathfrak{Re}(k_z)}{\partial k_x^2}}{\left\{1+\left(\dfrac{\partial\mathfrak{Re}(k_z)}{\partial k_x}\right)^2\right\}^{3/2}}\right|_{k_x^0} \tag{4}$$

for an isofrequency curve $k_z(k_x)$. The diffraction coefficient evaluated at $\mathbf{k}^{(0)}$ is a measure for the spreading or focusing of the beam along its mean propagation direction. If $D<0$ diffraction is normal, similar to an ordinary homogeneous medium, and if $D>0$ it is anomalous, observable, for instance, in waveguide arrays and photonic crystals. Concerning the refraction of a beam at an interface between two arbitrary media 1 and 2 (i.e., air and MM), the transverse wave-vector component k_x^0 has to be conserved. One can furthermore introduce the inclination parameter,

$$V(k_x^0) = \left.\frac{\partial\mathfrak{Re}(k_z)}{\partial k_x}\right|_{k_x^0} \tag{5}$$

which is related to the transverse shift that a beam experiences during propagation. If $V<0$, the beam is inclined into the $x+$ direction and vice versa. Hence, we may consider the refraction coefficient $R(k_x^0)=V_1(k_x^0)/V_2(k_x^0)$ which is a measure for refraction between media 1 and 2. The sign of R distinguishes between normal ($R>0$) and anomalous (negative) refraction ($R<0$). Thus we may conclude that the dependence of the quantities D, V, and R on the mean propagation vector $\mathbf{k}^{(0)}$ of the normal modes completely reflects the refraction and diffraction properties of any considered medium.

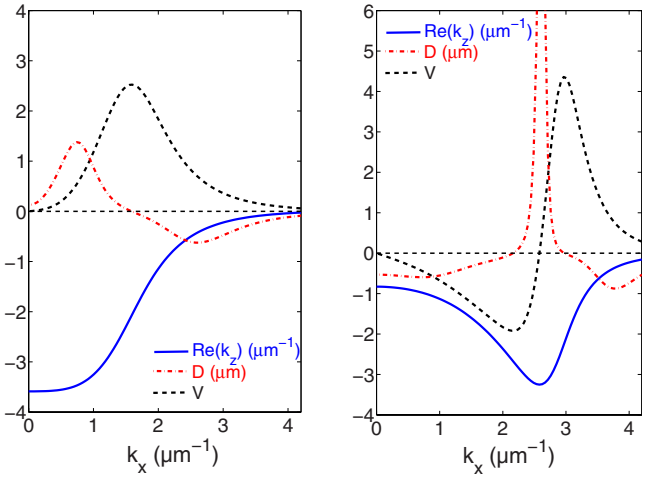

FIG. 5. (Color online) Isofrequency curves [real part of k_z (blue, solid curve)], the inclination parameter (V) (black, dashed curve), and the diffraction coefficient D (red, dashed-dotted curves) vs the transverse wave-vector component k_x. Left: $\lambda_1=1.437$ μm; right: $\lambda_2=1.389$ μm.

Now we return to the analysis of the isofrequency curves of the considered fishnet structure. Neglecting for a moment the imaginary part of the longitudinal effective wave-vector component k_z, Fig. 5 shows the relevant data. There, $\mathfrak{Re}[k_z(k_x)]$ as well as the diffraction coefficient $D(k_x)$ and the inclination parameter $V(k_x)$ are shown for the two wavelengths of interest ($\lambda_1=1.437$ μm and $\lambda_2=1.389$ μm).

It is evident that the diffraction coefficient experiences rapid variations and even changes sign for both wavelengths. Moreover, it can be seen that near normal-incidence ($k_x=0$) anomalous diffraction ($D>0$) occurs only for λ_1, whereas it is normal for λ_2. This will have important consequences for the imaging properties as will be shown later. The inclination parameter V does not exhibit a simple monotonic behavior in neither case as it would be expected for an isotropic medium and it also changes sign for λ_2 at $k_x=2.6$ μm^{-1}. As will be shown in Sec. IV, this feature will lead to a transition from a positive to a negative refraction behavior.

Recalling the functionality of the perfect lens, we already mentioned that *anomalous diffraction* is required ($D>0$). Recalling the dispersion relation of an ideal isotropic ($n=-1$) MM, $k_z=\mathrm{sgn}(n)\sqrt{n^2k_0^2-k_x^2}=-\sqrt{k_0^2-k_x^2}$, it is evident that this model medium precisely fulfills these conditions. It is this *anomalous diffraction* which cancels exactly the *normal diffraction* of the free space. Choosing the correct focal distance of the well-known perfect lens configuration (half of the slab thickness), the total diffractive spreading between the two focal points disappears. These simple considerations will facilitate the understanding of image formation and they will be the key in explaining the realistic imaging properties of the current fishnet structure operated at wavelengths λ_1 and λ_2, respectively. The detailed calculations picking up these issues will be provided in Sec. III B.

A. Diffraction and imaging of Gaussian beams

In what follows, we assume the z axis as the principal propagation direction. Without loss of generality, the source field is assumed to be Gaussian as

$$E_0(x) = A_0 \exp\left(-\frac{x^2}{\sigma_x^2}\right),$$

leading to a Gaussian angular spectrum

$$E_0(k_x) \propto \exp(-k_x^2/\sigma_k^2), \tag{6}$$

where $\sigma_k = 2/\sigma_x$ denotes the angular spectral width.

To characterize the imaging properties, a series of calculations with a varying spectral width σ_k was performed for normally and obliquely incident beams. The waist of the incident beam was located 1.2 μm in front of the MM slab, which has an overall thickness of 2.4 μm corresponding to 12 functional MM layers. In order to clearly distinguish the impact of different physical effects (damping and varying diffraction), we will compare three different scenarios characterized by three different MM transmission functions.

The first one is the *real scenario* which employs the complete complex transmission coefficient $T_R(k_x) = T(k_x)$, where all damping effects are accounted for. The second one is the *semireal scenario*, where damping is neglected so that effectively only $\mathfrak{Re}(k_z)$ will be taken into account, i.e., $T_{SR}(k_x) = \exp\{i \arg[T(k_x)]d\}$. The third one serves as a benchmark and is the *semi-ideal scenario*, assuming the dispersion relation of an effectively homogeneous and isotropic material having $n=-1$ (circular isofrequency curve). The complex transmission coefficient is approximated by $T_{SI}(k_x) = \exp\{-i\sqrt{\omega^2/c^2 - k_x^2}d\}$ with $k_x^2 \leq \omega^2/c^2$, representing essentially the perfect lens except the dropped evanescent waves.

B. Operating wavelength λ_1

The fishnet structure operated at a wavelength of 1.437 μm (see left panel of Fig. 5) exhibits an anomalous diffraction for $k_x < 1.6$ μm^{-1}, diffraction-free propagation at $k_x = 1.6$ μm^{-1}, and a normal diffraction beyond this point. Therefore, it is expected that the MM slab may work as a lens for normally incident beams with an angular spectrum $|k_x| < 1.6$ μm (this corresponds to a beam width of about $1.5\lambda_1$). Oblique incidence will lead either to a further spreading or a more complex behavior because some spectral components experience normal and some anomalous diffraction.

Table I provides an overview over the widths of the beams at the image focal position as a function of the spatial and angular width of the incident beam. The focal position is identified as the point where the amplitude reaches its unique maximum at the optical axis.

In the *semi-ideal scenario*, differences between input and output width can be clearly attributed to the missing evanescent waves. In the *semireal scenario* the width becomes larger than in the semi-ideal one if the angular spectrum becomes sufficiently broad ($|\sigma_k| \geq 1/10 \cdot 2\pi/\lambda_1$). First, we attribute this difference to the nonconstant curvature of $\mathfrak{Re}(k_z)$, leading to higher-order diffraction terms, which results in additional aberrations. These aberrations tend to increase the width of the image. These effects are very similar to the temporal propagation characteristics of pulses, where higher-order dispersion leads to pulse deformation and broadening.[22] Second, as already mentioned before, the diffraction is only anomalous (as required for focusing) for $k_x \leq 1.6$ μm^{-1}. Thus proper imaging can be expected as long as the angular spectrum is not too broad (beam not too narrow) ($|\sigma_k| \leq 1/3 \cdot 2\pi/\lambda_1$).

TABLE I. Calculated beam width (FWHM) in the focal plane of the MM slab for the different scenarios as described in the main body of the text for different incident-beam widths. Additionally the spectral width σ_k of the input beam is given. No clear focus position could be identified for the *real scenario* at $\sigma_k = 3/3 \cdot 2\pi/\lambda_1$.

σ_k in $2\pi/\lambda_1$	FWHM in units of λ_1			
	Input	Semi-ideal	Semireal	Real
1/10	5.33	5.33	5.33	6.47
1/6	3.21	3.21	3.27	4.86
1/3	1.59	1.59	1.70	3.97
2/3	0.79	0.85	1.32	3.74
1	0.53	0.71	1.21	

Now, in order to close the gap between ideal and real MMs, losses are fully taken into account (last column of Table I). The smallest achievable focal width amounts to about $3.74\lambda_1$. The large deviation to the *semireal scenario* may be explained by the strong variations of the imaginary part $\mathfrak{Im}(k_z)$ (Fig. 2), causing an inhomogeneous attenuation of the angular spectrum components. The MM acts essentially as a low-pass filter, which becomes evident in inspecting Fig. 3. The transmitted amplitude has its maximum at normal incidence ($T \sim 10^{-4}$) dropping rapidly to $T \sim 10^{-6}$ for $|k_x| = 1.7$ μm^{-1}, where the succeeding increase has no big effect (see the transmission function in a nonlogarithmic scale in the right panel of Fig. 6). The full width at half maximum (FWHM) of this central transmission peak is about 1.05 μm^{-1} corresponding to a spatial beam width (FWHM) of 5.1 μm (Gaussian shape assumed). This value fits perfectly to the calculations presented in Table I and is close to the aforementioned limit of about $3.74\lambda_1 = 5.37$ μm.

For the sake of visualization of the image formation, Fig. 6 shows the amplitude distribution behind the MM for the three scenarios (transmission functions), where two different source widths have been considered. In all cases $z=0$ coincides with the MM output facet.

The first and third rows display two distinct spectral widths σ_k of the input beam. The upper row belongs to $\sigma_k = 1/3 \cdot 2\pi/\lambda_1$ (FWHM$=1.59\lambda_1$) and the lower one to $\sigma_k = \pi/\lambda_1$ (FWHM$=0.53\lambda_1$).

It can be clearly seen from Fig. 6 that both focal width and position differ strongly where the latter changes significantly for the transition from the semi-ideal to the semireal or real scenario, respectively. As expected for the semi-ideal calculations, the focus is exactly located 1.2 μm behind the MM slab. For both the semireal and real calculations, the focal point is shifted further away ($\sim$9–11 μm). In the first approximation, this is caused by the quite large diffraction coefficient D in the interval of interest ($k_x < \sigma_k = 1/3 \cdot 2\pi/\lambda_1 = 1.46$ μm^{-1}) compared to the semi-ideal case.

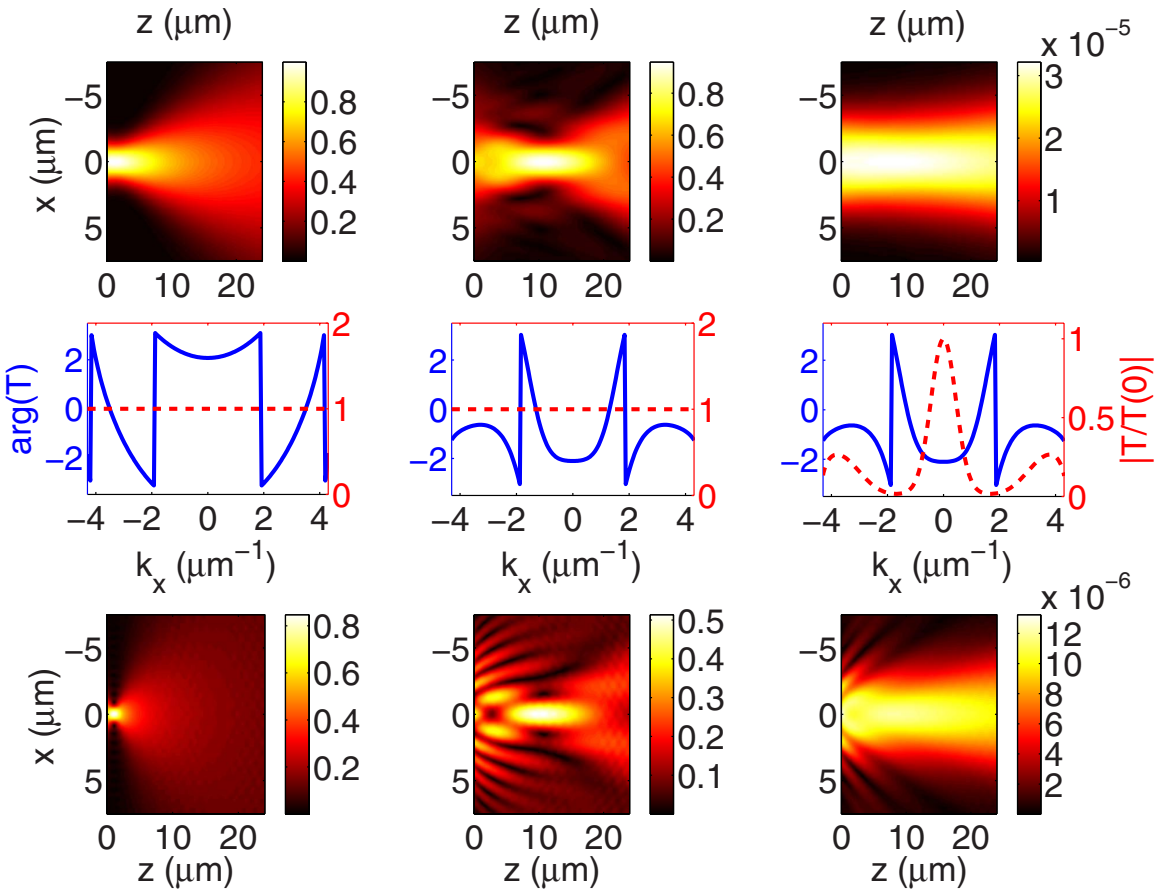

FIG. 6. (Color online) Amplitude distributions of the field transmitted through the MM slab at normal incidence for $\lambda_1=1.437$ μm. Top row: source's FWHM is $1.59\lambda_1$ ($\sigma_k=1/3\cdot 2\pi/\lambda_1$); bottom row: source's FWHM is $0.53\lambda_1$ ($\sigma_k=\cdot 2\pi/\lambda_1$). Middle row: phase (blue, solid) as well as the normalized modulus (red, dashed) of the respective MM slab transmission function. The different columns reflect the three different transmission functions used to calculate the field distributions. First column: T_{SI}; second column: T_{SR}; and third column: T_R.

There, the diffraction coefficient is constant with a value of $D=1/(k_0|n|)=1/k_0=0.23$ μm whereby it extends up to $D=1.38$ μm (see Fig. 5) for the semireal and real calculations, respectively. This would require a thinner MM for obtaining a focal spot near 1.2 μm. It remains to note that already in the semireal case (without losses) beam distortions are very strong. This indicates again the crucial effect of the nonspherical isofrequency curve on the imaging properties.

C. Operating wavelength λ_2

Now we study the case with the qualitatively different isofrequency curve at $\lambda_2=1.389$ μm, which exhibits a local maximum at normal incidence and a minimum at $k_x\simeq 2.60$ $\mu\mathrm{m}^{-1}$ [see Figs. 2 and 5 for the dispersion relation $k_z(k_x)$, the diffraction (D), and inclination coefficients (V), respectively]. Therefore the diffraction is normal ($D<0$) for $k_x<2.15$ $\mu\mathrm{m}^{-1}$ (see Fig. 5). Hence, normally incident beams cannot be focused by a MM slab at this frequency, although the derived refractive index is negative in the entire domain. This clearly demonstrates that a negative refractive index *is not sufficient* for using a MM slab as a focusing device, not to mention a perfect lens. Although not explicitly shown, this behavior was indeed proven by the numerical simulations of beam propagation. There is only a narrow domain (2.15 $\mu\mathrm{m}^{-1}<k_x<3.0$ $\mu\mathrm{m}^{-1}$) where *anomalous diffraction* occurs. Thus focusing may be achieved for obliquely incident beams, but due to the strong changes in the diffraction coefficient the imaging quality is expected to be poor. This has been numerically verified as can be recognized from Fig. 7. We assumed oblique incidence with a mean transverse wave vector of $k_x^0=2.4$ $\mu\mathrm{m}^{-1}$ for the illuminating Gaussian beam.

The comparison between the semi-ideal and the semireal calculations shows strong deviations of the beam's propagation characteristics behind the MM slab, where the white arrow marks the corresponding focus position. For an input beam with a FWHM of $4.24\lambda_2$, the image width is $4.25\lambda_2$ for the semi-ideal case calculated 1.2 μm behind the slab; whereas it amounts to $4.84\lambda_2$ measured at $z=31.68$ μm, in the semireal scenario. This rather large difference in the focal distance may be again attributed to the huge variation in the diffraction coefficient in the latter case near $k_x^0=2.4$ $\mu\mathrm{m}^{-1}$ (see Fig. 5, right).

Considering the real scenario, it is apparent that no focal point can be identified. Instead the smallest beam width is directly observed at the output facet ($z=0$) and amounts to FWHM$=6.34\lambda_2$. This behavior can again be attributed to the effect of the imaginary part $\Im\mathrm{m}(k_z)$ of the propagation con-

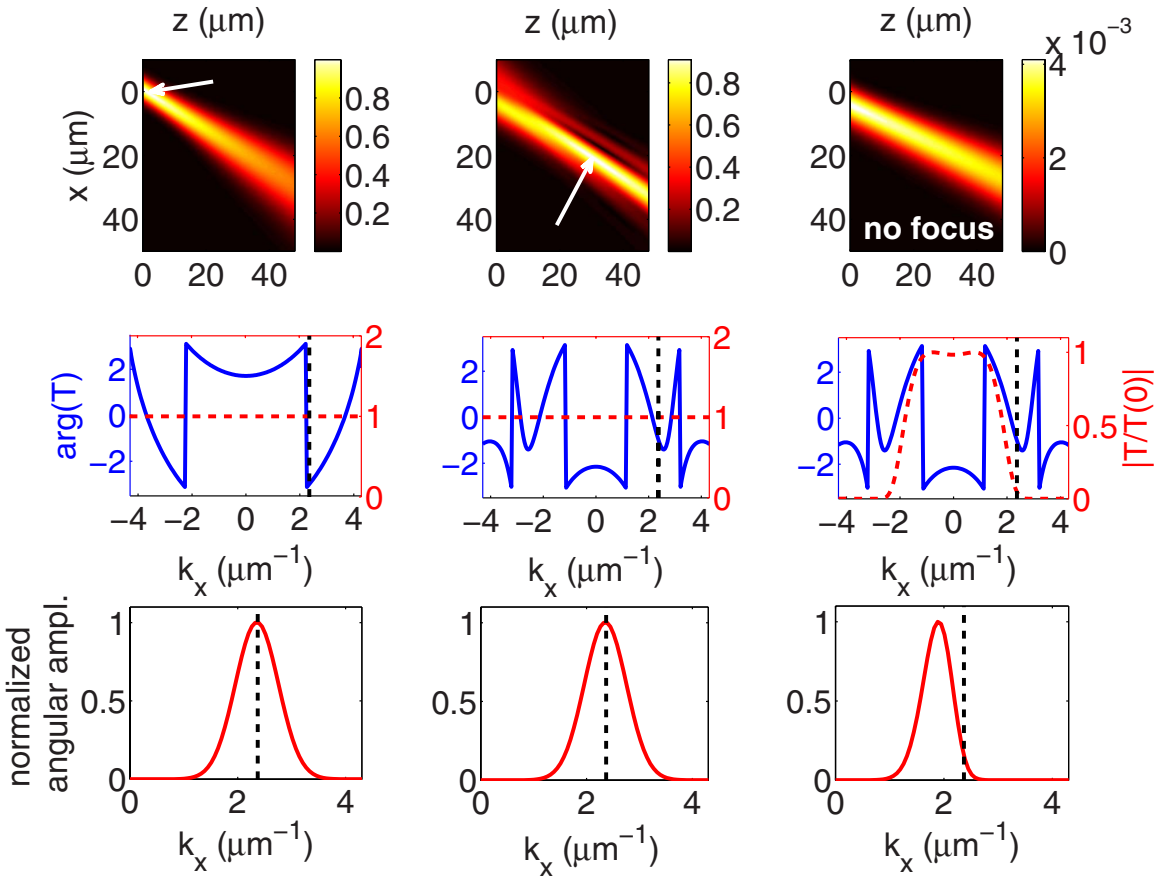

FIG. 7. (Color online) Top row: amplitude distributions of the field transmitted through the MM slab at oblique incidence $k_x^0 = 2.4\ \mu\text{m}^{-1}$ for $\lambda_2 = 1.388\,9\ \mu\text{m}$. The source's spectral width is $\sigma_k = 1/8 \cdot 2\pi/\lambda_2$ corresponding to a FWHM of $4.24\lambda_2$; middle row: phase (blue, solid) as well as the normalized modulus (red, dashed) of the respective MM slab transmission function; and bottom row: normalized angular spectrum of the transmitted field directly at the back facet ($z=0$) of the MM slab. The black dashed line indicates the mean transverse wave-vector component k_x^0 of the incident beam. The different columns reflect the three different transmission functions used to calculate the field distributions. First column: T_{SI}, second column: T_{SR}; and third column: T_R.

stant. In looking at Fig. 2 or at the left panel of Fig. 4, it can be seen that $\Im\text{m}(k_z)$ has a strong gradient between $k_x \sim 2\ \mu\text{m}^{-1}$ and $k_x \sim 3\ \mu\text{m}^{-1}$. If the structure is excited by a beam having its principal propagation direction within this angular spectral range, the spectrum of the beam is asymmetrically damped. Therefore, the first momentum of the spectrum and so the principal propagation direction is significantly shifted. In the present case, the shift occurs toward smaller values of k_x. This is illustrated in the third row of Fig. 7. The dashed vertical line indicates the mean transversal component of the wave vector of the incident field which is $k_x = 2.4\ \mu\text{m}^{-1}$. The presented curves show the angular spectrum of the normalized transmitted field. In contrast to the semi-ideal and the semireal calculations scenario, the angular center is shifted to $k_x \sim 1.95\ \mu\text{m}^{-1}$. Thus, the principal spectral component is now situated outside the anomalous diffraction regime (D becomes negative; compare Fig. 5) preventing focusing of the output field. Hence, the complex interplay between the effects caused either by the real or the imaginary part of the propagation constant hinders the image formation, although the beam spectrum was initially situated in the domain of anomalous diffraction. In general, at this wavelength, a genuine focusing effect could not be observed. Strong damping of waves in the angular domain where the diffraction coefficient is anomalous prevents refocusing of the beam.

D. Double Gaussian source field distribution

In the previous calculations, we have dealt with a single Gaussian beam incident onto the MM slab. To make contact with the standard resolution criteria in evaluating imaging properties, we proceed with two spatially separated Gaussian sources. The calculations are performed for either wavelengths, where a free-space propagation (MM is replaced by air) over equal distance serves as a benchmark. The source field consists of two Gaussian distributions of angular width $\sigma_k = 1/3(2\pi/\lambda)$ $(\rightarrow \sigma_x = 2/\sigma_k = 3\lambda/\pi)$ spatially separated by a distance $2S_x$. By this, the field is written as

$$E_0(x) \propto \exp\left[-\frac{(x-S_x)^2}{\sigma_x^2}\right] + \exp\left[-\frac{(x+S_x)^2}{\sigma_x^2}\right].$$

The source position is $1.2\ \mu\text{m}$ in front of the MM.

At first, the left part of Fig. 8 shows the results for $\lambda_1 = 1.438\ \mu\text{m}$. Here the separation $2S_x$ of the Gaussians amounts to $6\ \mu\text{m}$. The red dashed curve represents the re-

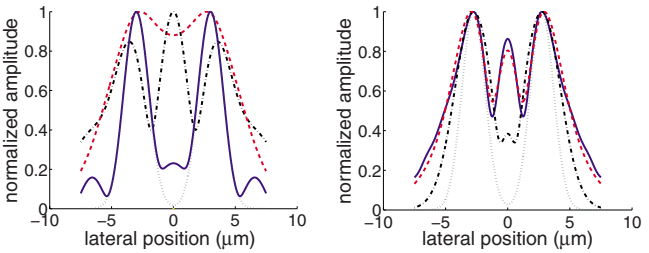

FIG. 8. (Color online) Normalized image of two spatially separated Gaussian fields (parameters in the text) for $\lambda_1=1.438$ μm at the focal point $z=10$ μm (left) and $\lambda_2=1.389$ μm at $z=1.2$ μm (right). The different curves correspond to: input field (green, dotted), semireal propagation (blue, solid), real propagation (red, dashed), and pure free-space propagation (black, dashed dotted). In case of $\lambda_1=1.438$ μm, the image positions correspond to the identified focal positions of the beams in Sec. III B. The field for free-space propagation is evaluated at the same position. In case of $\lambda_2=1.389$ μm, an arbitrary position was chosen because no genuine backside focus could be identified.

sults of the real propagation scenario. Although two distinct maxima are properly visible (compare to the input field distribution), the MM lens is working at its resolution limit because the contrast to the central minimum is almost vanishing. Considering the semireal calculation (blue, solid), it is certainly not surprising that it clearly reproduces the main features of the source field distribution. The black dashed-dotted curve shows the diffraction pattern revealed for a free-space propagation over the same distance. Summarizing these observations it can be noticed that the resolution of the real MM lens is very much affected by the strong dispersive absorption properties, although the essential features of the object can be still identified.

Second, the right part of Fig. 8 shows the results for $\lambda_2=1.389$ μm, where we do not expect the MM lens to work properly. As it was discussed in the previous example, we can meaningfully analyze the imaging characteristics only in comparing them to a free-space propagation of equal distance (up to 1.2 μm behind the slab). In doing so, a free-space propagation over (in sum) 4.8 μm still keeps the two main maxima of the source field distribution because the overall diffraction is sufficiently small. On the other hand it can be seen that in case of the semireal and real calculations, the overall diffraction is higher, resulting i.e., in an additional amplitude maximum in the center. As expected at normal incidence, the functionality of the fishnet slab operated at $\lambda_2=1.389$ μm is even worse compared to a similar free-space propagation.

IV. REFRACTION OF BEAMS AND THEIR TRANSVERSE SHIFT

A beam propagating through any medium experiences diffraction. On the contrary, beam refraction appears only at the interface of two media. In this section, we shall show that one can likewise take advantage of the dispersion relation to explain the refraction effects at MM surfaces. It has been shown that interesting effects appear in reflection, as, e.g.,

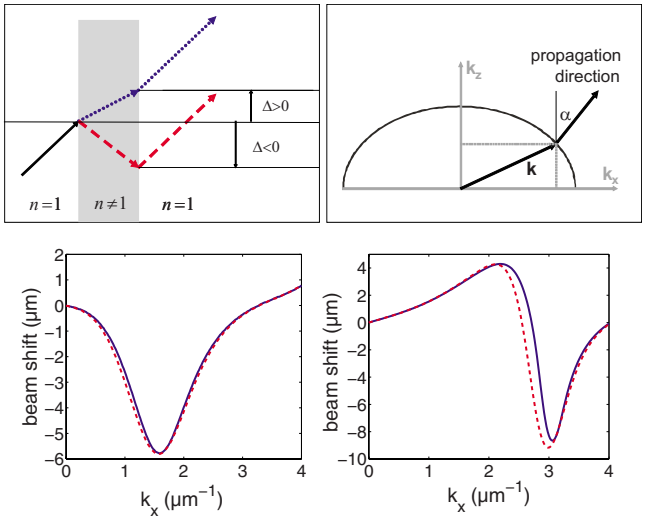

FIG. 9. (Color online) Refraction of wide beams. Top left: schematic picture of ray optical refraction and beam shift at the interfaces of an isotropic and homogeneous slab for oblique incidence. In geometrical optics, a material with $\Re\mathfrak{e}(n)>0$ leads to a *positive* shift of the beam $\Delta>0$ (blue, dotted path) along the surface. For $\Re\mathfrak{e}(n)<0$ the expected shift is *negative*, with $\Delta<0$ (red, dashed path). Top right: schematic illustration of the direction of beam propagation normal to the isofrequency curve around the mean wave vector $\mathbf{k}^{(0)}$ (lossless medium assumed). Bottom: calculated beam displacements Δ of the transmitted field at the output facet of the MM slab as a function of the incident-beam's mean wave-vector component k_x^0. The incident beam is Gaussian with $\sigma_k=1/25\cdot 2\pi/\lambda(\mathrm{FWHM}\approx 19$ μm). Left: operational wavelength $\lambda_1=1.437$ μm; right: operational wavelength $\lambda_1=1.389$ μm. Semireal case T_{SR}: (red, dashed); real case T_R (blue, solid).

the Goos-Hänchen and/or the Imbert-Fedorov shift.[23,24] Here it will turn out that peculiarities may also occur in transmission.

For example, it is well known that an obliquely incident beam, traversing a slab, experiences a displacement caused by refraction at both interfaces. In geometrical optics, light is represented by rays, which are refracted at material boundaries, as described by Snell's law. By considering a beam of light impinging from vacuum and traversing a homogeneous and isotropic slab, the sign of the observed beam displacement Δ is strictly related to the sign of the real part of the slab's refractive index $\Re\mathfrak{e}(n)$. This is illustrated in the top panel of Fig. 9. In this simple yet intuitive picture, multiple reflections inside the slab structure are neglected. In case of a slab material with a relatively large damping rate, which holds for the considered fishnet structure, this assumption appears to be realistic.

By contrast, in wave optics a monochromatic beam of light can be represented by its angular spectrum centered around its main wave vector $\mathbf{k}^{(0)}=(k_x^0,k_z^0)^T$ provided that $k_y=0$. For a lossless medium, the mean propagation direction (energy flow) of a beam points normal to the isofrequency contour $(\partial\omega/\partial\Re\mathfrak{e}[\mathbf{k}^{(0)}])$.[25] Therefore, the beam's propagation angle α is linked to the already introduced inclination parameter $V(k_x^0)$ by $\tan[\alpha(k_x^0)]=-V(k_x^0)=-\partial\Re\mathfrak{e}(k_z)/\partial k_x|_{k_x^0}$. Now, we consider the beam refraction at an arbitrary interface between

two media. If the beam hits the interface, the transverse wave-vector component k_x^0 passes continuously. The respective longitudinal component k_z^0, and thus likewise the propagation direction of the refracted beam, is adjusted by the dispersion relation of the medium where the beam enters. For refraction into photonic crystals, these considerations are well established and are used to explain the superprism effect or negative refraction.[26,27] Thus only if the medium is homogeneous and isotropic (spherical or circular isofrequency surface), simple Snell's law may be applied but it fails in all other cases. In other words, the refractive index $n(k_x^0)$ evaluated only at the central wave-vector component is no longer a measure for refraction. Instead, the inclination parameter or the refraction coefficient has to be used. If strong losses [large $\Im\mathfrak{m}(k_z)$] are involved, as in the present fishnet MM, similar angular filtering effects as already discussed in Sec. III can be observed. However, using sufficiently wide and paraxial beams, the losses can be considered constant in the narrow angular spectral range of interest and the whole beam experiences a constant damping during propagation with negligible impact on the beam's profile. Nevertheless, in the following calculations the influence of damping will be considered and its consequences are pointed out.

We shall study refraction at the fishnet MM slab where we take advantage of the results displayed in Fig. 5 (isofrequency curve $\Re\mathfrak{e}[k_z(k_x)]$ and inclination parameter $V(k_x^0)$ for the two relevant wavelengths $\lambda_1=1.437$ μm and $\lambda_2=1.389$ μm). For both wavelength, the refractive index would be negative in the whole angular spectral domain (see blue curves in Fig. 5), thus one would naively expect negative refraction in the entire domain. However, it will turn out that the inclination coefficient V in the MM is the relevant quantity that controls refraction. For $\lambda_1=1.437$ μm (see Fig. 5 left) V is positive, exhibiting a maximum at $k_x \sim 1.6$ $\mu\mathrm{m}^{-1}$. This leads to the conclusion that anomalous refraction should appear (negative beam displacement $\Delta<0$) in the entire angular domain. To verify this statement, rigorous numerical calculations are performed for a Gaussian beam with $\sigma_k=1/25\cdot 2\pi/\lambda$ and a mean wave vector (and thus the incident angle) which varies from normal to grazing incidence. The beam displacement is simply measured as the difference of the beam's center of gravity at the front and the back side facet of the MM slab, respectively. The results of two different computational scenarios (real case—T_R and semireal case—T_{SR}) are shown in Fig. 9 (bottom left). Both curves almost coincide indicating that the variation of $\Im\mathfrak{m}(k_z)$ is of minor importance as long as the beam's spectrum is sufficiently small. Losses affect only the transmittance but not the refraction. The numerical results agree almost perfectly with the predictions derived from the inclination parameter V in Fig. 5. The maxima of both functions coincide and the beam displacement is entirely negative except for $k_x^0>3.5$ $\mu\mathrm{m}^{-1}$, where rigorous calculations predict a slight positive beam displacement. This can be attributed to the Fresnel effects at the boundary, which become important for large incident angles. They lead to the modifications of the amplitude transmission function across the spectral width of the incident beam (the logarithm of the transmitted amplitude tends to diverge toward $-\infty$ for grazing incidence; see Fig. 3).

As expected from the isofrequency curve and the inclination parameter V at $\lambda_2=1.389$ μm (see Fig. 5, right panel), refraction is expected to change from normal to anomalous behavior at $k_x^0>2.6$ $\mu\mathrm{m}^{-1}$. This is indeed confirmed by rigorous numerical calculations (see Fig. 9, bottom right). For smaller incident angles, the refraction is normal and the beam displacement is positive. This is a very instructive example for the irrelevance of the retrieved refractive index, which is negative in the entire parameter region (see Fig. 2; bottom left, green curve). On the other hand, the predictions based on the dispersion relation (Fig. 5) and rigorous calculations (Fig. 9) agree perfectly.

V. CONCLUSIONS

We have shown that diffraction, refraction, and imaging of beams at MM slabs may be comprehensively explained and understood on the basis of the dispersion relation of light in the respective medium. It turns out that the isofrequency curves are quite complex and neither spherical nor elliptical. This may lead to variations between normal and anomalous refraction and diffraction behaviors, respectively. Thus the analyzed MM does not mimic an isotropic or a uniaxial or biaxial anisotropic medium. In this context it turned out that the concept of an effective refractive index is pointless in the mesoscopic operational domain of contemporary MMs because simple geometric optical models, such as Snell's law, are no longer appropriate. Only the complete dispersion relation provides access to the correct description of all relevant effects. To this end, related quantities as inclination and diffraction coefficients may be introduced. They may be used to predict (de-)focusing and imaging of narrow beams as well as normal or anomalous refraction of wide beams. Concerning the imaging properties of a realistic fishnet MM slab, the specific dispersion properties prevent ideal imaging (perfect lens) of narrow beams, regardless of evanescent waves which are completely damped by absorption. We have also found that diffraction and inclination coefficients are strongly dispersive. Thus, e.g., a blue shift of the wavelength from the resonance at normal incidence may prevent any image formation. Refraction may behave normal even in domains with a negative effective index. All the predictions based on the dispersion relation have been numerically verified by rigorous calculations. In designing MMs for perfect lens applications, we suggest to optimize the MM with respect to an almost constant anomalous diffraction coefficient rather than with respect to a large negative refractive index.

ACKNOWLEDGMENTS

The authors acknowledge support by the Federal Ministry of Education and Research (Metamat) and the Deutsche Forschungsgemeinschaft. Some computations utilized the IBM p690 cluster (JUMP) of the Forschungszentrum in Jülich, Germany.

*Corresponding author: thomas.paul@uni-jena.de

[1] J. B. Pendry, Phys. Rev. Lett. **85**, 3966 (2000).
[2] J. B. Pendry, D. Schurig, and D. R. Smith, Science **312**, 1780 (2006).
[3] A. M. Nicolson and G. F. Ross, IEEE Trans. Instrum. Meas. **19**, 377 (1970).
[4] D. R. Smith, S. Schultz, P. Markoš, and C. M. Soukoulis, Phys. Rev. B **65**, 195104 (2002).
[5] A. I. Căbuz, D. Felbacq, and D. Cassagne, Phys. Rev. A **77**, 013807 (2008).
[6] C. Menzel, C. Rockstuhl, T. Paul, F. Lederer, and T. Pertsch, Phys. Rev. B **77**, 195328 (2008).
[7] C. Rockstuhl, C. Menzel, T. Paul, T. Pertsch, and F. Lederer, Phys. Rev. B **78**, 155102 (2008).
[8] D. N. Christodoulides, F. Lederer, and Y. Silberberg, Nature (London) **424**, 817 (2003).
[9] R. Iliew, C. Etrich, and F. Lederer, Opt. Express **13**, 7076 (2005).
[10] G. Dolling, M. W. Klein, M. Wegener, A. Schädle, B. Kettner, S. Burger, and S. Linden, Opt. Express **15**, 14219 (2007).
[11] D. R. Smith and D. Schurig, Phys. Rev. Lett. **90**, 077405 (2003).
[12] W. T. Lu and S. Sridhar, Phys. Rev. B **77**, 233101 (2008).
[13] C. Rockstuhl, T. Paul, F. Lederer, T. Pertsch, T. Zentgraf, T. P. Meyrath, and H. Giessen, Phys. Rev. B **77**, 035126 (2008).
[14] E. Noponen and T. Turunen, J. Opt. Soc. Am. A Opt. Image Sci. Vis **11**, 2494 (1994).
[15] L. Li, J. Opt. Soc. Am. A Opt. Image Sci. Vis **13**, 1024 (1996).
[16] L. Li, J. Opt. Soc. Am. A Opt. Image Sci. Vis **13**, 1870 (1996).
[17] G. Dolling, C. Enkrich, M. Wegener, C. Soukoulis, and S. Linden, Opt. Lett. **31**, 1800 (2006).
[18] N. Liu, L. Fu, S. Kaiser, H. Schweizer, and H. Giessen, Adv. Mater. (Weinheim, Ger.) **20**, 3859 (2008).
[19] Permittivity of silver: $\epsilon_{\mathrm{Ag}}=1-\omega_p^2/(\omega^2+ig\omega)$, with $\omega_p=1.37\times10^{16}$ s^{-1} and $g=8.5\times10^{13}$ s^{-1}.
[20] V. G. Veselago, Sov. Phys. Usp. **10**, 509 (1968).
[21] K. Aydin, I. Bulu, and E. Ozbay, Appl. Phys. Lett. **90**, 254102 (2007).
[22] G. P. Agrawal, *Nonlinear Fiber Optics* (Cambridge University Press, Cambridge, 1999).
[23] C. Menzel, C. Rockstuhl, T. Paul, S. Fahr, and F. Lederer, Phys. Rev. A **77**, 013810 (2008).
[24] T. Paul, C. Rockstuhl, C. Menzel, and F. Lederer, Phys. Rev. A **77**, 053802 (2008).
[25] E. Sakoda, *Optical Properties of Photonic Crystals* (Springer, New York, 2001).
[26] T. Baba, T. Matsumoto, and M. Echizen, Opt. Express **12**, 4608 (2004).
[27] C. Luo, S. G. Johnson, J. D. Joannopoulos, and J. B. Pendry, Phys. Rev. B **65**, 201104(R) (2002).